



**HAL**  
open science

# An end-to-end pipeline based on open source deep learning tools for reliable analysis of complex 3D images of Medaka ovaries

Manon Lesage, Jérôme Bugeon, Manon Thomas, Thierry Pécot, Violette Thermes

## ► To cite this version:

Manon Lesage, Jérôme Bugeon, Manon Thomas, Thierry Pécot, Violette Thermes. An end-to-end pipeline based on open source deep learning tools for reliable analysis of complex 3D images of Medaka ovaries. 2022. hal-03759490

**HAL Id: hal-03759490**

**<https://hal.science/hal-03759490v1>**

Preprint submitted on 24 Aug 2022

**HAL** is a multi-disciplinary open access archive for the deposit and dissemination of scientific research documents, whether they are published or not. The documents may come from teaching and research institutions in France or abroad, or from public or private research centers.

L'archive ouverte pluridisciplinaire **HAL**, est destinée au dépôt et à la diffusion de documents scientifiques de niveau recherche, publiés ou non, émanant des établissements d'enseignement et de recherche français ou étrangers, des laboratoires publics ou privés.



Distributed under a Creative Commons Attribution - NonCommercial - NoDerivatives 4.0 International License

# 1 **An end-to-end pipeline based on open source deep learning tools**

## 2 **for reliable analysis of complex 3D images of Medaka ovaries**

3 Manon Lesage<sup>1,#</sup>, Jérôme Bugeon<sup>1</sup>, Manon Thomas<sup>1</sup>, Thierry Pécot<sup>2</sup>, Violette Thermes<sup>1,#</sup>

4 <sup>1</sup>INRAE, Fish Physiology and Genomics Institute, 16 Allee Henri Fabre, Rennes 35000, France.

5 <sup>2</sup>BIOSIT, UAR 3480 US 018, Université de Rennes 1, 2 rue Professeur Leon Bernard, Rennes 35042,  
6 France

7  
8 # Corresponding authors

### 9 10 **Keywords:**

11 Fish, reproduction, N2V, Cellpose, confocal microscopy, 3D imaging, optical tissue clearing,  
12 Deep learning segmentation, Artificial Intelligence

### 13 14 **Short title:**

15 A deep-learning based workflow to assess the ovarian oocyte content in Medaka

### 16 17 **Summary statement**

18 An accessible image analysis method for biologists, which includes easy-to-use deep learning  
19 algorithms, designed for accurate quantitative measurement of ovarian content from complex  
20 3D fluorescent images.

### 21 22 **Grants support :**

23 The DYNAMO project (Agence National de la Recherche, ANR-18-CE20-0004).

24 The IMMO project (grants from the INRAE Metaprogramme DIGIT-BIO).

### 25 26 **Corresponding authors:**

27 [manon.lesage@inrae.fr](mailto:manon.lesage@inrae.fr)

28 [violette.thermes@inrae.fr](mailto:violette.thermes@inrae.fr)

29 INRAE, Laboratoire de Physiologie et Génomique des poissons, Campus de Beaulieu, 35042

30 Rennes cedex, France

31

## 32 **ABSTRACT**

33 Computational analysis of bio-images by deep learning (DL) algorithms has made  
34 exceptional progress in recent years and has become much more accessible to non-  
35 specialists with the development of ready-to-use tools. The study of oogenesis  
36 mechanisms and female reproductive success in fish has also recently benefited from the  
37 development of efficient three-dimensional (3D) imaging protocols on entire ovaries.  
38 Such large datasets have a great potential for the generation of new quantitative data on  
39 oogenesis but are, however, complex to analyze due to imperfect fluorescent signals and  
40 the lack of efficient image analysis workflows. Here, we applied two open-source DL tools,  
41 Noise2Void and Cellpose, to analyze the oocyte content of medaka ovaries at larvae and  
42 adult stages. These tools were integrated into end-to-end analysis pipelines that include  
43 image pre-processing, cell segmentation, and image post-processing to filter and combine  
44 labels. Our pipelines thus provide effective solutions to accurately segment complex 3D  
45 images of entire ovaries with either irregular fluorescent staining or low autofluorescence  
46 signal. In the future, these pipelines will be applicable to extensive cellular phenotyping  
47 in fish for developmental or toxicology studies.

48

## 49 INTRODUCTION

50 As imaging methods for thick biological samples improve and become more widespread in  
51 various fields of life sciences, the volume of image data keeps growing and their analysis  
52 becomes even more complex. Biologists are therefore facing a rising need for computational  
53 tools to analyze large bio-image datasets and extract reproducible and meaningful biological  
54 information.

55 The fish ovary is a complex organ that shows important structural and functional changes  
56 during reproductive cycles. It contains different types of cells, including oocytes (*i.e.*, female  
57 gametes) and numerous surrounding somatic supporting cells that form, together with each  
58 oocyte, the functional units known as ovarian follicles (Lubzens et al., 2010; Nakamura et al.,  
59 2009). During oogenesis, each follicle grows and differentiates until finally giving rise to eggs  
60 that are ultimately released during spawning. One of the greatest challenges facing research on  
61 the development of ovarian dynamics and functions is the lack of an effective method to  
62 accurately count growing oocytes regardless of their stage. Studies have indeed traditionally  
63 been limited to automatic or manual oocyte counting on two-dimensional (2D) ovarian sections  
64 and extrapolation of the data to the whole organ or to manual counting of dissociated follicles  
65 (Gay et al., 2018; Iwamatsu, Takashi, 1978; Iwamatsu, 2015). Some studies have also focused  
66 on the development of complex stereological approaches to limit the biases induced by 2D  
67 approaches (Charleston et al., 2007). Recently, the emergence of optical tissue clearing methods  
68 and powerful microscopes have opened new perspectives with the possibility of imaging whole  
69 ovaries in three dimensions (3D), notably for mice and fishes (Fiorentino et al., 2021; Lesage  
70 et al., 2020; Soygur and Laird, 2021). It is thus now possible to generate 3D image data,  
71 generally of very large size, that ideally allows direct and comprehensive access to all structures  
72 and to achieve a precise 3D image reconstruction of the whole ovary. However, tools for 3D  
73 image analyses are still too inaccurate and tedious, especially for image segmentation, partly

74 because of an irregular contrast signal in depth and the presence of oocytes of heterogenous  
75 sizes, as reported previously for the adult Medaka ovary (Lesage et al., 2020). Ovarian 3D  
76 imaging therefore has a promising future, but its widespread use still relies on the availability  
77 of more efficient and easier-to-use computerized analytical tools.

78 In recent years, artificial intelligence (AI) has developed considerably and is proving to be  
79 highly effective for digital image analysis in biology, which has recently led to a deluge of  
80 publications in this field. Various algorithms based on deep learning (DL) have emerged and  
81 provide many applications in microscopy allowing to overcome classical limitations such as  
82 image segmentation. They allow to increase object recognition accuracy, segmentation  
83 reproducibility and enable to save a considerable amount of time for the analysis of large  
84 datasets by limiting manual interventions of users (Moen et al., 2019). Some specific methods  
85 have thus been proposed to automatically segment follicles in the mammalian ovary from  
86 histological 2D sections using a convolutional neural network (CNN) (Inik et al., 2019; Sonigo  
87 et al., 2018). Other more generalist tools have recently emerged to democratize the use of DL  
88 technology with few prerequisites in computed coding, by providing either DL trained models  
89 accessible from public databases (<https://bioimage.io/#/>), notebooks accessible from any  
90 computer (von Chamier et al., 2021), or other open-source plugins such as CSBDeep (Weigert  
91 et al., 2018) or DeepImageJ (Gómez-de-Mariscal et al., 2021). Among the available models for  
92 cell segmentation, Cellpose is a particularly versatile one, providing a generalist pre-trained  
93 model for segmentation that can perform on various cell types in a great variety of acquisition  
94 modalities (Stringer et al., 2021). Cellpose has recently proven to be very effective in  
95 segmenting muscle fibers from 2D images of histological sections (Waisman et al., 2021).  
96 Noise2Void (N2V) is another approach that stands out for its image denoising performance.  
97 N2V does not require noisy image pairs nor clean target images, therefore allowing training  
98 directly on the corpus of data to be denoised (Krull et al., 2019). In the era of deep learning, it

99 thus appears that some of the routine limitations for bio-image analysis are now solved. All that  
100 remains for the biologist is the delicate task of integrating deep learning steps into the various  
101 analytical procedures for 2D and for 3D images in particular.

102 The aim of this study was to test the possibility of using a pre-trained open-source model to  
103 improve the critical step of segmentation of Medaka ovary 3D images without undergoing the  
104 fastidious and complex task of neural network training. We generated 3D fluorescent images  
105 of the adult ovarian follicle boundaries, by using the Methyl Green nuclear dye. We also  
106 generated 3D images of ovaries at the larvae stage, by using the autofluorescence signal in  
107 oocyte cytoplasm. For 3D segmentation of both types of images, we applied the generalist  
108 Cellpose model for oocyte 3D segmentation, which was even more efficient after image pre-  
109 processing steps and N2V denoising. A post-processing step after Cellpose was also set up to  
110 eliminate any remaining error and to combine labels when necessary. N2V and Cellpose have  
111 thus been integrated into a complete pipeline that allows an accurate estimation of the oocyte  
112 content from complex 3D images of the whole Medaka ovary.

113

## 114 **MATERIAL AND METHODS**

### 115 **Ethical Statement**

116 All fish were reared in the INRAE ISC-LPGP fish facility, which hold full approval for animal  
117 experimentation (C35-238-6). All fish were handled in strict accordance with French and  
118 European policies and guidelines of the INRAE LPGP Institutional Animal Care and Use  
119 Committee (no.M-2020-126-VT-ML, no.M-2019-48-VT-SG).

120

### 121 **Medaka breeding and sample collection**

122 Medaka fish (*Oryzias latipes*) from the CAB strain were raised at 26°C under artificial  
123 photoperiod dedicated to growth phase (16 h light/ 8 h dark) or reproductive cycles (14 h light/

124 10 h dark). Female fish were sampled either at larvae stage (20 days post-hatch, dph) or adult  
125 stage (5 months old). Fish were euthanized by immersion in a lethal dose of MS-222 at 300mg/L  
126 supplemented with NaHCO<sub>3</sub> at 600mg/L and fixed overnight at 4°C in 4% paraformaldehyde  
127 (PFA) diluted in 0.01 M phosphate buffer saline (PBS) pH 7.4. Larvae were then dehydrated  
128 gradually in methanol and stored at -20°C. Adult ovaries were dissected after fixation and  
129 directly stored at 4°C in PBS + 0.5% (w/v) sodium azide (S2002, Sigma-Aldrich).

130

### 131 **Fluorescent staining and clearing**

132 Larvae were progressively rehydrated in PBS and ovaries were dissected. Ovaries were then  
133 permeabilized and immunostained following the iDISCO protocol with some modifications  
134 (Renier et al., 2014). Samples were successively incubated in PBS/0.2% Triton X-100 (PBSTx)  
135 for 30 min twice, PBSTx/20% DMSO for 30 min at 37°C and in PBSTx/0.1% Tween-20/20%  
136 DMSO/0.1% deoxycholate/0.1% NP40 at 37 °C for 3 h. Ovaries were washed in PBSTx for 15  
137 min twice, then blocked in PBS/0.1% Triton X-100/20% DMSO/6% Sheep Serum for 2H30-  
138 3H at 37°C. Samples were immunolabelled with anti-phospho-Histone H3 (Ser10) primary  
139 antibody (1:500, 06-570 Merck millipore), washed for 0.5 day in PBS/0.1% Tween-20/10µg/ml  
140 heparin (PBSTwH) under gentle agitation, and incubated with Alexa-Fluor 546 secondary  
141 antibody (1:500, A11035, ThermoFisher). Antibodies incubations were conducted for 2.5 days  
142 at 37°C in PBSTwH/5% DMSO/3% Sheep serum. Finally, stained larvae ovaries were  
143 embedded in low-melting agarose 1% before proceeding to clearing. Adult ovary samples were  
144 stained and cleared according to the C-ECi method with few modifications (Lesage et al., 2020).  
145 For staining, adult ovaries were incubated with the Methyl Green dye (MG) (40 µg/mL, 323829,  
146 Sigma-Aldrich) in PBS/0.1% Triton X-100 at 37°C for 2.5 days. After Staining, both adult  
147 ovaries and embedded larvae ovaries were dehydrated in serial methanol/H<sub>2</sub>O dilution series  
148 supplemented with Tween-20 (2% and 0.1%, respectively), then immersed in 100% ethyl-3-

149 phenylprop-2-enoate (ethyl cinnamate [ECi]) (W243000, Sigma-Aldrich) and finally kept at  
150 room temperature until subsequent imaging step.

151

## 152 **Samples mounting and imaging**

153 Image acquisitions were performed with a Leica TCS SP8 laser scanning confocal microscope  
154 equipped with a 16x/0.6 IMM CORR VISIR HC FLUOTAR objective (ref. 15506533, Leica,  
155 Wetzlar, Germany). For larvae ovaries, samples embedded in agarose blocks were glued on a  
156 coverslip and placed in a glass Petri dish filled with ECi. Adult ovaries were successively placed  
157 with ventral side up or down for complete imaging despite the objective working distance  
158 limitation, and mounted as described previously (Lesage et al., 2020). Mosaic z-stack tiles were  
159 stitched in Leica software using 11,72% overlap. Larvae ovaries were acquired in 1024x1024  
160 pixels, 400Hz (unidirectional) with an optical zoom of 1.3 and a z-step of 1.63  $\mu\text{m}$  (voxel size  
161 0.52 x 0.52 x 1.6264  $\mu\text{m}$ ). PH3 fluorescent signal was acquired using 552 nm laser excitation  
162 slightly above optimal intensity (3-4%), and frame average was set to 2. Acquisitions took  
163 between 1.5 and 5.5 hrs according to ovary size and generated 1 to 2 GB of data. Adult ovaries  
164 were acquired in 512x512 pixels, 600Hz (bidirectional), optical zoom 0.75, z-steps 6  $\mu\text{m}$  (voxel  
165 size 1.80 x 1.80 x 6.00  $\mu\text{m}$ ), line accumulation 2 and frame average 2. Ventral and dorsal z-  
166 stacks were acquired in about 10 hrs each and generated 8 to 10 GB of data. MG staining was  
167 detected with 638 nm laser and excitation gain compensation was used along Z axis (5 to 10%  
168 intensity).

169

## 170 **Image processing**

171 A schematic overview of image treatment workflows is shown on Figure 1. All steps were  
172 conducted on the open-source FIJI software, unless otherwise specified.

173



174 ***Image intensity and contrast enhancement***

175 Before image enhancement, adult z-stacks were downscaled in order to reduce computation  
176 time. A resampling factor of 3 on X and Y axes was used, which resulted in images sizes of  
177 1214 x 970 pixels. Progressive intensity and gamma correction plugin was applied along the Z  
178 axis to compensate fluorescence loss in depth (Fig. 1B). For larvae, exponential or linear  
179 interpolation method were used with default parameters and intensity enhancement was set  
180 between 150 and 400% depending on samples. For adults, linear interpolation method was used,  
181 intensity set between 200 and 800% and normalization was selected (modifying range of pixel  
182 intensity values by linear scaling method). A linear gamma correction was also performed  
183 (factor 1.5) to enhance mid tones pixels on adult images. Image contrast was then enhanced by  
184 applying Contrast Limited Adaptive Histogram Equalization (CLAHE) with following  
185 parameters: block size 128, bins 256, slope 3 and fast mode, for larva; block size 512, bins 256,  
186 slope 30 and fast mode, for adult. A Fiji macro was used to apply this function on Z-stacks by  
187 batches, which is available on our GitHub page: [https://github.com/INRAE-](https://github.com/INRAE-LPGP/ImageAnalysis_CombineLabels)  
188 [LPGP/ImageAnalysis\\_CombineLabels](https://github.com/INRAE-LPGP/ImageAnalysis_CombineLabels).

189

190 ***3D registration***

191 Adult ventral and dorsal 3D stacks were registered, aligned and combined with the FijiYama  
192 plugin using the “two images registration mode (training)” (Fig. 1B). A manual registration was  
193 first performed to roughly superimpose the two volumes. Automatic registration was then  
194 applied for linear image transformation with block-matching alignment method. Linear  
195 transformations included rigid transformations (translation and rotation) and, if necessary,  
196 similarities transformations (rigid and isotropic homothetic factor). The two registered stacks  
197 were fused with Image calculator (Max operator), resulting in image size of 1324 x 1108 x 713  
198 pixels.

199

## 200 ***Signal-to-noise ratios enhancement***

201 Three-dimensional images were denoised using Noise2Void (N2V) deep-learning based tool  
202 available on Fiji, using a model trained on a few selected 3D stacks snippets. A 2D model was  
203 trained on folder containing ~15 Z-stacks snippets (512x512, from 50 to 115 z-steps) cropped  
204 from different larvae samples. Training patch shape was set at 96x96 pixels and N2V  
205 automatically used data augmentation (90, 180 and 270 rotations and flipping), thereby  
206 multiplying total patches amount by 8. The resulting pool of 2D patches were used for training  
207 (90%) and validation (10%). Training was performed with 250 epochs, 150 steps/epoch and  
208 batch size set to 128, resulting in ~13 hrs of training with our computer specifications.  
209 Denoising prediction duration was estimated to ~12 min for 1GB of data with our stated  
210 parameters (batch size 2). For adult, similar strategy was used for training, using 10 z-stack  
211 snippets (256x256, 100-200 Z-steps), patch shape 64x64 pixels. Training was performed with  
212 300 epochs, 200 steps/epoch, batch size 128, for a total of ~9 hrs of training. Denoising  
213 prediction duration was estimated to ~8 min for 1GB of data with our hardware specifications  
214 and stated parameters (batch size 2). For image edges enhancement, stacks were subjected to a  
215 3D median filter (x,y,z radius 1,1,1 for larvae and 2,2,2 for adult). Filtered image was then  
216 subjected to external morphological gradient computation (shape: ball; x,y,z radius 3,3,3 for  
217 larvae and 2,2,2 for adult) with Morphological filters (3D) function of MorpholibJ plugin.  
218 External gradient image was then subtracted from original pre-treated stack (without median  
219 filtering). An internal morphological gradient was also computed on larvae stacks (element  
220 shape: ball, x,y,z radius 4,4,4) and added to image data. For 3D visualization of data, volume  
221 reconstructions were performed on the Amira software using Volren rendering (Fig 2A, E) or  
222 Volume-rendering (Fig 3A, F and 4A, F).

223

## 224 ***Deep learning 3D segmentation***

225 Follicle segmentation was performed using Cellpose algorithm with local environment  
226 installation, launched from Anaconda command prompt (Fig. 1C). For larvae, X and Y scale  
227 were first reduced by half so that mean follicle diameter approach ~30 pixels, which is the  
228 optimum diameter for Cellpose cell segmentation (final image size 1194 x 610 pixels). Cellpose  
229 was then run in 3D with “cyto” pre-trained model, setting parameters as follows: diameter 30,  
230 cellprob threshold -2, anisotropy 1,6, min size 10. A batch size of 2 was used, depending on  
231 GPU memory allocation, resulting in ~50 min for segmentation prediction of ~250 Mb of data.  
232 Resulting masks were saved in TIFF format for subsequent data treatment. For adults, the same  
233 process was used except anisotropy was set to 1.7. 3D segmentation took ~4 hrs for ~1 Gb of  
234 data. To segment out-of-range follicles, adult stacks were downscaled once more by applying  
235 a resampling factor of 2 in X, Y and Z (no interpolation, final images size of 662 x 554 x 357  
236 pixels). Downscaled stacks were subjected to Cellpose segmentation with diameter size set to  
237 30 and 60 pixels. 3D segmentation took ~35 min and ~11 min for ~125 Mb of downsized data,  
238 for 30 and 60 pixel diameter respectively.

239

## 240 ***Post-processing and data extraction***

241 For post-processing of segmented follicles, data were first slightly narrowed. For that operation,  
242 label boundaries were computed with MorpholibJ plugin and subtracted from the original  
243 Cellpose results. For larvae ovary images, labels were then post-processed on AMIRA software.  
244 Labels were subjected to an opening morphological operator (3 pixels, precise) and then filtered  
245 based on their size (Equivalent Diameter  $\geq 1.5e-5m$ ) and shape (ShapeVAa3d  $\leq 3.5$ ). Few  
246 remaining errors were manually corrected. For adult ovary images, label shrinkage, filtration  
247 and combination were performed automatically or semi-automatically using a Fiji macro.  
248 Labels were filtered based on volume and sphericity parameters. When necessary, segmentation

249 images were rescaled to match 3D registered image size (1324 x 1108 x 713px). The  
250 combination strategy consisted in adding largest segmented labels from downscaled images  
251 (using Cellpose diameter 30) on original scale label segmentation (Cellpose diameter 30) where  
252 largest follicles were over-segmented (Supplemental Fig. 1). Briefly, labels  $>650\mu\text{m}$  volume-  
253 equivalent diameter (EqDiameter) were filtered from the downscaled image and added to the  
254 original scale label image after selection and deletion (using morphological reconstruction  
255 operation) of wrong labels resulting from over-segmentation. For combination of missing  
256 largest labels, a similar strategy was used with downscaled label image obtained with Cellpose  
257 diameter 60, but with semi-automatic method. Missing labels were manually selected with  
258 multi-point tool and then processed as presented before. Macro “CombineLabels” was  
259 developed in IJ1 Macro language and can be downloaded from the Github page:  
260 [https://github.com/INRAE-LPGP/ImageAnalysis\\_CombineLabels](https://github.com/INRAE-LPGP/ImageAnalysis_CombineLabels). The volumes of all  
261 segmented follicles were exported and equivalent diameters were calculated. For adults,  
262 EqDiameter were subjected to a correction factor of 1.12 to compensate the volume shrinkage  
263 due to sample clearing, as described in Lesage *et al.* (Lesage et al., 2020). Data analysis was  
264 performed on labels above 25 and 50  $\mu\text{m}$  in diameter, for larvae and adult samples respectively.  
265 Label 3D reconstructions were generated on Amira using volume-rendering object.

266

## 267 **Hardware and software**

268 Data were analyzed on a 64-bit Windows 10 Pro computer equipped with a 2x Intel Xeon Silver  
269 4110 (8 Cores, 3.0GHz) processor, a Nvidia Geforce GTX 1080 graphic card, and 384 Go of  
270 RAM. We used the Amira 2020.2 software with the XLVolume extension (Thermo Fisher  
271 Scientific, Waltham, Massachusetts, United States), Anaconda3-2021.11 python distribution,  
272 Python 3.7.9, CUDA toolkit 10.0, PyTorch 1.6.0 and Cellpose v0.6.1 (Stringer et al., 2021).  
273 We also used FIJI (Schindelin et al., 2012) and the following plugins: CLAHE (Pizer et al.,

274 1987; Zuiderveld, 1994), Progressive intensity and gamma correction (Murtin, 2016), FijiYama  
275 (fijiYama-4.0.0) (Fernandez and Moisy, 2021), CLIJ2 (clij2-2.5.3.0, Haase et al., 2020),  
276 MorpholibJ (morpholibJ-1.4.3, Legland et al., 2016), Noise2Void (n2v-0.8.6)(Krull et al.,  
277 2019) and CSBDeep (csbdeep-0.6.0)(Weigert et al., 2018).

278

## 279 **RESULTS**

### 280 **3D imaging of the ovaries**

281 To detect oocytes within the ovary at both adult and larvae stages, sample were  
282 fluorescently stained and optically cleared to allow full imaging by confocal fluorescence  
283 microscopy (Fig. 1A). For adult ovaries, nuclei of supporting cells surrounding the oocytes  
284 were stained with the fluorescent nuclear dye Methyl-Green (MG) identified as a convenient  
285 marker for delineating follicle boundaries (Lesage et al., 2020). For larvae ovaries (20 dph),  
286 which are composed of small early developing oocytes flanked by only a few supporting  
287 somatic cells, we took advantage of the cytoplasmic autofluorescence generated by  
288 immunostaining (here anti-phospho-histone H3 antibody, PH3). Resulting images displayed a  
289 very low signal-to-noise ratio (SNR) and a rapid loss of signal recovery in depth for larvae  
290 ovaries (Fig. 2A-D). Signal intensity was twice as low at 440  $\mu\text{m}$  in depth compared to the top  
291 (150  $\mu\text{m}$  depth, Fig. 3B, B'). In addition, it is noteworthy that smaller oocytes were less  
292 distinguishable than larger ones having thicker cytoplasm, especially in very compact regions  
293 (Fig. 2D and 3B). Images stacks of adult ovaries displayed a higher fluorescence signal with a  
294 high SNR that was recovered up to 1152  $\mu\text{m}$  in depth, although some heterogeneity in  
295 fluorescence intensity was observable (Fig. 2F, G). At a greater depth (2 000  $\mu\text{m}$ ), images  
296 display a substantial loss of signal intensity (Fig. 4B, B').

297

### 298 **Image enhancement and 3D visualization**

299 Given the uneven signal intensity of the images, and especially the very low SNR observed  
300 with the non-specific staining of larval ovaries, we applied successive processing steps to  
301 enhance the fluorescent signal throughout Z-stacks prior segmentation. For larvae ovary,  
302 fluorescence intensity of image stacks was progressively enhanced along Z-axis to increase the  
303 signal in depth, and mean grey values were increased and homogenized to enhance contrasts  
304 (Fig. 3B, B', C, C'). To minimize the noise potentially introduced by intensity and contrasts  
305 adjustment and to avoid potential aberrant enhancement of noisy structures, image stacks were  
306 denoised using the self-supervised N2V deep-learning-based algorithm (Krull et al., 2019) (Fig.  
307 3D, D'). Finally, edges were refined using morphological gradients (Fig. 3E, E'). XY views  
308 from Z-stacks and fluorescent intensity profiles through adjacent oocytes show the progressive  
309 signal recovery over the different steps at both 150 and 440  $\mu\text{m}$  in depth. It is noticeable that  
310 while normalizing grey values distribution, N2V denoising preserves oocytes edges with  
311 limited blurring effect, thus minimizing any feature loss (Fig. 3D, D'). In addition, it is  
312 noteworthy that overexposure was created in some cases as a side effect of edge refinement.  
313 The challenge here was therefore to find a compromise between the loss of detection of  
314 underexposed oocytes and the overexposure generated in order to achieve the greatest  
315 difference between light and dark levels. Image pre-processing steps thus enabled to increase  
316 the overall fluorescent signal intensity, to better define edges of the oocytes and to homogenize  
317 the fluorescence intensity across the Z-stack, thereby allowing a better 3D reconstruction of the  
318 larval ovary (Fig. 3A, F).

319 For 3D images of adult ovaries, a similar strategy was applied except an extra step of  
320 automatic 3D registration that was performed for the reconstruction of the whole ovary (Fig.  
321 4B-E and 4B'-E'). As a result of the combination of images in the overlap region, 3D  
322 registration led to a slight increase in fluorescence intensity in this region in the final stack (Fig.  
323 4A, F). XY views of Z-stacks and fluorescent intensity profiles through adjacent oocytes

324 showed a significant increase of the SNR, especially at 2 000  $\mu\text{m}$  in depth. Similar to the larvae  
325 ovary, the pre-processing allowed to improve the fluorescence signal, and especially to  
326 homogenize the fluorescence intensity through the Z-stack for a better 3D reconstruction of the  
327 adult ovary (Fig. 4A, F).

328

### 329 **Cellpose efficiently identifies oocytes and follicles on 3D images**

330 For 3D oocyte and follicle segmentation on larvae and adult images, we selected the open-  
331 source Cellpose deep-learning algorithm because of its generalist nature for cell segmentation  
332 (Stringer et al., 2021). We compared the efficiency of Cellpose for 3D segmentation before and  
333 after image pre-treatment. In both cases, Cellpose could detect either internal fluorescent  
334 staining (oocyte cytoplasm) or external fluorescent staining (somatic follicular cells), on larvae  
335 and adult ovary images respectively (Fig. 5A-D and 5E-H). Notably, Cellpose was much more  
336 efficient on pre-treated images than raw images. Although XZ views of larvae stacks revealed  
337 accurate segmentation along the Z axis, several undetected oocytes and some Z-label fusions  
338 were detectable in the absence of preprocessing (Fig. 5B and 5D, insets). For adult ovaries,  
339 segmentation of raw images leads to many cases of over-segmentation in conjunctive tissues or  
340 in large follicles, as well as fewer detected follicles, compared to segmentation of pre-processed  
341 images (Fig. 5F and 5H, insets).

342

### 343 **Post-processing of label images after Cellpose 3D segmentation**

344 Cellpose output images were post-processed to adjust the label sizes to that of the oocytes (label  
345 shrinkage) and to remove outliers (label filtration) (Fig. 6). Label shrinkage was performed by  
346 automatically subtracting the label boundaries to the original Cellpose labels. For adult ovaries  
347 that have the unique feature of containing heterogeneous follicle sizes (ranging from about 20  
348 to 1 000  $\mu\text{m}$  in diameter), different Cellpose label images were generated by modulating image

349 resolution of the input image (Fig.6B, C). If necessary, a 60 pixel diameter was used for  
350 Cellpose segmentation to detect largest follicles. The different resulting label images were  
351 combined in an additional post-processing step by using a Fiji Macro named “CombineLabels”  
352 (Fig. 6D). Images of larvae ovary labels show that, after post-processing, the majority of labels  
353 perfectly fit to the shape and size of the oocytes and that aberrant labels with elongated shapes  
354 or very small sizes were removed. In few cases, some inaccuracies still persisted, mainly under-  
355 segmentation of small oocyte clusters (Fig. 6A, arrows) or non-segmented oocytes (Fig. 6A,  
356 arrowhead). Similar to larvae ovary images, results of segmentation and post-processing of  
357 adult ovary images were highly accurate, both in terms of follicle detection, label shape and  
358 size fitting (Fig. 6B-D). After post-processing, remaining segmentation errors were limited to  
359 a few outlier labels located outside the relevant structures.

360

## 361 **Oocyte content analyses**

362 To assess the ovarian oocyte content at both larvae and adult stages, ovaries were imaged at  
363 each of these stages and 3D computational analyses were performed following our deep  
364 learning-based pipeline. Three-dimensional reconstructions after data pre-processing revealed  
365 the thin oval-shape of larvae ovaries oriented along the anteroposterior axis, which then evolves  
366 into a thicker rounded shape at the adult stage (Fig. 3F, 4F, 7A and 7D). Ventrally, larvae  
367 ovaries exhibited lateral folds and a marked central depression, likewise adult ovaries displayed  
368 two lateral folds as well as a ventro-median bulge, giving the ovary a wheat grain appearance.  
369 Diameters of segmented oocytes or follicles were computed, classified into different size  
370 classes and merged to the 3D ovary reconstructions (Fig. 7A', B, D', E). The ventral and dorsal  
371 3D views of the larvae ovary, revealed that small oocytes were preferentially visible from the  
372 ventral views, whereas larger oocytes were only observable from dorsal views, while no  
373 obvious regionalization was observable in the adult ovary (Fig. 7B and 7E). To analyze the



374 relative abundance of the different size classes, the developmental stage of oocytes/follicles  
375 was determined according to their diameter and as described in the oocyte developmental table  
376 of Iwamatsu *et. al.* (Iwamatsu et al., 1988). In the larvae ovary, a total of  $1231 \pm 182$  (n=2)  
377 oocytes were detected. The mean size distribution showed a high predominance of small  
378 previtellogenic follicles ranging from 25 to 60  $\mu\text{m}$  in diameter (chromatin-nucleolar stage, stage  
379 I), which suggests a synchronized oocyte growth during larval development (Fig. 7C). By  
380 contrast, all follicular developmental stages were found at the adult stage. A total of 1275  
381 follicles were counted with a large predominance of pre-vitellogenic follicles (from stage II to  
382 IV, 50-150  $\mu\text{m}$ ) and of early vitellogenic follicles (stages V and VI, 150-400  $\mu\text{m}$ , Fig. 7F).  
383 Proportion of follicles then progressively decrease as they progress through late vitellogenesis  
384 (stages VII and VIII, 400-800  $\mu\text{m}$ ). The pool of post-vitellogenic follicles (maturation stage IX,  
385  $> 800 \mu\text{m}$ ) is clearly distinguishable and reflects upcoming egg laying with a consistent number  
386 of about 23 follicles measuring more than 950  $\mu\text{m}$  in diameter.

387

## 388 **DISCUSSION**

389 Three-dimensional imaging of whole fish ovaries typically generates large image data sets that  
390 are particularly complex to analyze. In this study, we generated two types of 3D images. On  
391 the one hand, we generated images of adult fish ovaries with low-contrast follicle outline signal  
392 at great depths, which usually greatly impairs the final segmentation efficiency, as described  
393 previously (Lesage et al., 2020). On the other hand, we generated images of larvae ovaries with  
394 a low-contrast signal inside the oocytes throughout image stacks, which makes segmentation  
395 otherwise impossible with conventional approaches. Here, we applied the generic Cellpose pre-  
396 trained algorithm that allows cell segmentation without any manual annotation and neural  
397 network training. To optimize 3D segmentation results and maximize accuracy of  
398 oocyte/follicle content analyses, Cellpose was integrated into an end-to-end analysis pipeline.

399

## 400 **Enhancement and homogenization of input dataset**

401 The first part of our pipeline was dedicated to signal quality improvement in depth of raw image  
402 stacks. Such image pre-processing steps allowed improving segmentation efficiency by  
403 Cellpose. To some extent, the decrease in fluorescence level in depth on raw images should not  
404 be a major issue for predicting feature boundaries with Cellpose as it uses vector gradients  
405 representation of objects to accurately predict complex cell outlines with non-homogenous cell  
406 marker distribution (Stringer et al., 2021). However, our result indicates that the SNR is an  
407 important prerequisite for image analysis with Cellpose, in line with previous observations (Kar  
408 et al., 2021). Along with an enhanced visualization of the structures of interest across the  
409 sample, the pre-processing of 3D images therefore allows for homogenization of the data set  
410 and much more efficient 3D segmentation with Cellpose, thus increasing the reproducibility  
411 and quality of analysis.

412

## 413 **Improvement of Cellpose output label images**

414 Despite its high efficiency, Cellpose led to some substantial errors, including slightly oversized  
415 or aberrant labels, and it also failed to segment oocytes of highly heterogeneous sizes. To  
416 overcome these limitations and refine labels produced by Cellpose, we performed post-  
417 segmentation corrections. The size of 3D labels was adjusted following an automated boundary  
418 subtraction strategy. Our strategy differs from other methods that use the pixel-by-pixel label  
419 erosion operation, such as in LabelsToROIs Fiji plugin designed on 2D myofiber sections, and  
420 is likely to be faster when dealing with large 3D data (Waisman et al., 2021). The combination  
421 of multiple Cellpose segmentation images, implemented with a Fiji macro “CombineLabels”,  
422 also allows identification of highly heterogeneous objects sizes, that was previously not  
423 possible with Cellpose algorithm alone. It is however worth noting that there are still few

424 inaccuracies that could not be fixed. Under-segmentations or unsegmented objects were  
425 sometimes detected mostly with larvae image datasets. Albeit minor, these errors occur in  
426 highly oocyte-dense regions or with non-optimal signal levels. Such observation is in agreement  
427 with some studies that do not recommend Cellpose for highly overlapping masks or that  
428 describe lower accuracy with over- or underexposed images (Kar et al., 2021). This could be  
429 attributed to the 2D averaging process for the 3D Cellpose extension that may have lower  
430 accuracy than a model trained with 3D data, especially for highly dense regions (Lalit et  
431 al.,2022; Stringer et al., 2021). Obviously, one can assume that better accuracy could be  
432 achieved by using a dedicated specialized DL model, and in particular with 3D trained model  
433 on our data, as shown by D.Eschweiler et *al* (Eschweiler et al., 2022). It would thus be  
434 interesting in the future to use our segmentation results for Cellpose algorithm fine-tuning. This  
435 could indeed limit the need for image pre-processing as well as post-processing corrections of  
436 segmentation results. But in this case, we would somewhat lose the advantage of versatile  
437 generalist models like Cellpose and different models would have to be trained for each type of  
438 data. Another solution could therefore be to improve the input images quality, by using a  
439 suitable oocyte marker to avoid sharp signal enhancement and possibly in combination with a  
440 membrane marker for better boundary discrimination. Alternatively, and in absence of such  
441 specific staining, another denoising process, either trained in three dimensions, with noisy/non-  
442 noisy paired images (CARE) or combining deconvolution process (DecoNoising), could also  
443 help objects recognition accuracy (Weigert et al., 2018; Goncharova et al., 2020).

444

## 445 **An accurate and comprehensive content analysis of larvae and adult medaka** 446 **ovaries**

447 Implementation of Cellpose for oocytes/follicle 3D segmentation eventually enabled unbiased,  
448 reproducible and comprehensive studies for meaningful biological information, which offers

449 great possibilities for a complete description of fish ovarian growth and development. From a  
450 morphological point of view, we could clearly distinguish the oval shape of the ovary  
451 thickening over time and shaping a bulge in the ventro-median position that connects the  
452 mesentery and attaches to the gut (Iwamatsu, 2015; Lesage et al., 2020). *In situ* follicular size  
453 measurements by our 3D imaging and DL-based segmentation approaches allowed producing  
454 size distribution profiles for both larvae and adult ovaries. Our results are consistent with those  
455 obtained previously from dissociated follicles measured manually for the larvae ovary  
456 (Iwamatsu, 2015) or semi-automatically from 3D images by classical watershed segmentation  
457 approaches for the adult ovary as shown in our previous study (Lesage et al., 2020). However,  
458 greater confidence can be attributed to the present study, particularly for the pre- and post-  
459 vitellogenic stages in the adult ovary for which we achieved fewer segmentation errors. In  
460 general, we also achieved a better estimation of follicle size due to the accurate shape detection  
461 enabled by the Cellpose algorithm. Interestingly, we also noticed that the spatial distribution of  
462 oocytes between 30 and 70  $\mu\text{m}$  in diameter tended to be regionalized along the ventro-dorsal  
463 axis in the larvae ovary, suggesting an oriented follicular growth through this axis in  
464 consistency with observation of Nakamura *et al.* (Nakamura, 2018). In the future, the ovarian  
465 morphogenesis and spatial organization of follicles according to their size should however be  
466 further characterized during the ovarian development by using refined 3D spatial analysis  
467 approaches.

468

## 469 **Conclusion**

470 Overall, the use of the generic Cellpose algorithm has been successful for 3D ovary images and  
471 has allowed ovarian segmentation of unprecedented quality. Cellpose significantly accelerated  
472 and improved the efficiency and the quality of ovarian follicles 3D segmentation in adults,  
473 leading to an accurate count and measurement of all oocyte diameters. Even more remarkably,

474 this generalist model also allowed the successful segmentation of images of larvae ovaries with  
475 weak fluorescent signal, otherwise not exploitable with conventional methods, and quite  
476 certainly even after image pre-processing. This possibility challenges the dogma that a good  
477 raw image is necessary for an accurate object segmentation and thus significantly increases  
478 further analysis opportunities. Furthermore, thanks to its ease of use, implementation of  
479 Cellpose avoids the tedious and complex step of setting up an AI segmentation method and is  
480 therefore largely accessible to non-specialist biologists with limited coding and hardware  
481 knowledge. In the deep learning era, it is thus now clearly possible to apply such a cutting-edge  
482 technology for tissue 3D phenotyping with relative ease. To our knowledge, our pipeline is the  
483 first application using developer-to-user deep learning solutions for 3D image analysis of the  
484 ovary in vertebrates, thus opening the way for further innovative in-depth morphometric studies  
485 within the framework of developmental or toxicological studies.

486

## 487 **ACKNOWLEDGMENTS**

488 We thank the INRAE ISC-LPGP fish facility staff and especially Amélie Patinote and  
489 Guillaume Gourmelen for fish rearing and husbandry.

490

## 491 **ADDITIONAL INFORMATION AND DECLARATIONS**

### 492 **Funding**

493 This work was funded by The DYNAMO project (Agence Nationale de la Recherche, ANR-  
494 18-CE20-0004 to V.T.). This work has also been supported by the IMMO project (grants from  
495 the INRAE Metaprogramme DIGIT-BIO to V.T.). The funders had no role in study design, data  
496 collection and analysis, decision to publish, or preparation of the manuscript.

497

498 **Competing Interests**

499 The authors declare there are no competing interests.

500

501 **Author Contributions**

502 M.L. performed the experiments, the computational analyses and wrote the manuscript.

503 J.B. participated to the setup of the computation bio-image analyses. M.T. participated in

504 the setup of the clearing protocol and to the image acquisition. T.P. participated in the

505 choice and implementation of the tool for the 3D registration of adult ovary images. V.T.

506 conceived the study, participated in data analyses and manuscript writing. All authors

507 reviewed drafts of the article and approved the final manuscript.

## 508 REFERENCES

- 509
- 510 **Charleston, J. S., Hansen, K. R., Thyer, A. C., Charleston, L. B., Gougeon, A., Siebert, J.**  
511 **R., Soules, M. R. and Klein, N. A.** (2007). Estimating human ovarian non-growing follicle  
512 number: the application of modern stereology techniques to an old problem†. *Human*  
513 *Reproduction* **22**, 2103–2110.
- 514 **Eschweiler, D., Smith, R. S. and Stegmaier, J.** (2022). Robust 3D Cell Segmentation:  
515 Extending the View of Cellpose.
- 516 **Fernandez, R. and Moisy, C.** (2021). FijiYama: a registration tool for 3D multimodal time-  
517 lapse imaging. *Bioinformatics* **37**, 1482–1484.
- 518 **Fiorentino, G., Parrilli, A., Garagna, S. and Zuccotti, M.** (2021). Three-dimensional  
519 imaging and reconstruction of the whole ovary and testis: a new frontier for the reproductive  
520 scientist. *Molecular Human Reproduction* **27**, gaab007.
- 521 **Gay, S., Bugeon, J., Bouchareb, A., Henry, L., Montfort, J., Le Cam, A., Bobe, J. and**  
522 **Thermes, V.** (2018). MicroRNA-202 (miR-202) controls female fecundity by regulating  
523 medaka oogenesis.
- 524 **Gómez-de-Mariscal, E., García-López-de-Haro, C., Ouyang, W., Donati, L., Lundberg,**  
525 **E., Unser, M., Muñoz-Barrutia, A. and Sage, D.** (2021). DeepImageJ: A user-friendly  
526 environment to run deep learning models in ImageJ. *Nat Methods* **18**, 1192–1195.
- 527 **Goncharova, A. S., Honigmann, A., Jug, F. and Krull, A.** (2020). Improving Blind Spot  
528 Denoising for Microscopy.
- 529 **Haase, R., Royer, L. A., Steinbach, P., Schmidt, D., Dibrov, A., Schmidt, U., Weigert,**  
530 **M., Maghelli, N., Tomancak, P., Jug, F., et al.** (2020). CLIJ: GPU-accelerated image  
531 processing for everyone. *Nat Methods* **17**, 5–6.
- 532 **İnik, Ö., Ceyhan, A., Balcioğlu, E. and Ülker, E.** (2019). A new method for automatic  
533 counting of ovarian follicles on whole slide histological images based on convolutional neural  
534 network. *Computers in Biology and Medicine* **112**, 103350.
- 535 **Iwamatsu, T.** (2015). Growth of the Medaka (IV) - Dynamics of Oocytes in the Ovary  
536 During Metamorphosis. *Bulletin of Aichi Univ. of Education* **64**, 37–46.
- 537 **Iwamatsu, T., Ohta, T., Oshima, E. and Sakai, N.** (1988). Oogenesis in the Medaka  
538 *Oryzias latipes* : Stages of Oocyte Development : Developmental Biology. *Zoological Science*  
539 **5**, 353–373.
- 540 **Iwamatsu, Takashi, T.** (1978). Studies on Oocyte Maturation of the Medaka, *Oryzias latipes*  
541 VI. RELATIONSHIP BETWEEN THE CIRCADIAN CYCLE OF OOCYTE  
542 MATURATION AND ACTIVITY OF THE PITUITARY GLAND. *J. Exp. Zool.* **206**, 355–  
543 364.
- 544 **Kar, A., Petit, M., Refahi, Y., Cerutti, G., Godin, C. and Traas, J.** (2021). *Assessment of*  
545 *deep learning algorithms for 3D instance segmentation of confocal image datasets.*  
546 *Bioinformatics.*
- 547 **Krull, A., Buchholz, T.-O. and Jug, F.** (2019). Noise2Void - Learning Denoising from  
548 Single Noisy Images. *arXiv:1811.10980 [cs]*.
- 549 **Lalit, M., Tomancak, P. and Jug, F.** Embedding-based instance segmentation in  
550 microscopy. *PMLR* 399–415.
- 551 **Legland, D., Arganda-Carreras, I. and Andrey, P.** (2016). MorphoLibJ: integrated library  
552 and plugins for mathematical morphology with ImageJ. *Bioinformatics* btw413.
- 553 **Lesage, M., Thomas, M., Bugeon, J., Branthonne, A., Gay, S., Cardona, E., Bobe, J. and**  
554 **Thermes, V.** (2020). *C-Eci: A Cubic-Eci Combined Clearing Method For 3D Follicular*  
555 *Content Analysis In The Fish Ovary.* Developmental Biology.
- 556 **Lubzens, E., Young, G., Bobe, J. and Cerdà, J.** (2010). Oogenesis in teleosts: how eggs are  
557 formed. *Gen. Comp. Endocrinol.* **165**, 367–389.

558 **Moen, E., Bannon, D., Kudo, T., Graf, W., Covert, M. and Van Valen, D.** (2019). Deep  
559 learning for cellular image analysis. *Nat Methods* **16**, 1233–1246.  
560 **Murtin, C. I.** (2016). Three-dimensional image analysis of high resolution confocal  
561 microscopy data of the *Drosophila melanogaster* brain. *Image Processing [eess.IV]*.  
562 **Université de Lyon.**, 1–166.  
563 **Nakamura, Y. T.** (2018). All Oocytes Attach to the Dorsal Ovarian Epithelium in the Ovary  
564 of Medaka, *Oryzias latipes*. *Zoological Science* **35**, 306–313.  
565 **Nakamura, S., Kurokawa, H., Asakawa, S., Shimizu, N. and Tanaka, M.** (2009). Two  
566 distinct types of theca cells in the medaka gonad: germ cell-dependent maintenance of  
567 *cyp19a1*-expressing theca cells. *Dev. Dyn.* **238**, 2652–2657.  
568 **Pizer, S. M., Amburn, E. P., Austin, J. D., Cromartie, R., Geselowitz, A., Greer, T. and**  
569 **Zuiderveld, K.** (1987). Adaptive Histogram Equalization and Its Variations. *COMPUTER*  
570 *VISION, GRAPHICS, AND IMAGE PROCESSING* 355–368.  
571 **Renier, N., Wu, Z., Simon, D. J., Yang, J., Ariel, P. and Tessier-Lavigne, M.** (2014).  
572 iDISCO: A Simple, Rapid Method to Immunolabel Large Tissue Samples for Volume  
573 Imaging. *Cell* **159**, 896–910.  
574 **Schindelin, J., Arganda-Carreras, I., Frise, E., Kaynig, V., Longair, M., Pietzsch, T.,**  
575 **Preibisch, S., Rueden, C., Saalfeld, S., Schmid, B., et al.** (2012). Fiji: an open-source  
576 platform for biological-image analysis. *Nature Methods* **9**, 676–682.  
577 **Sonigo, C., Jankowski, S., Yoo, O., Trassard, O., Bousquet, N., Grynberg, M., Beau, I.**  
578 **and Binart, N.** (2018). High-throughput ovarian follicle counting by an innovative deep  
579 learning approach. *Sci Rep* **8**, 13499.  
580 **Soygur, B. and Laird, D. J.** (2021). Ovary Development: Insights From a Three-  
581 Dimensional Imaging Revolution. *Front. Cell Dev. Biol.* **9**, 698315.  
582 **Stringer, C., Wang, T., Michaelos, M. and Pachitariu, M.** (2021). Cellpose: a generalist  
583 algorithm for cellular segmentation. *Nat Methods* **18**, 100–106.  
584 **von Chamier, L., Laine, R. F., Jukkala, J., Spahn, C., Krentzel, D., Nehme, E., Lerche,**  
585 **M., Hernández-Pérez, S., Mattila, P. K., Karinou, E., et al.** (2021). Democratising deep  
586 learning for microscopy with ZeroCostDL4Mic. *Nat Commun* **12**, 2276.  
587 **Waisman, A., Norris, A. M., Elías Costa, M. and Kopinke, D.** (2021). Automatic and  
588 unbiased segmentation and quantification of myofibers in skeletal muscle. *Sci Rep* **11**, 11793.  
589 **Weigert, M., Schmidt, U., Boothe, T., Müller, A., Dibrov, A., Jain, A., Wilhelm, B.,**  
590 **Schmidt, D., Broaddus, C., Culley, S., et al.** (2018). Content-aware image restoration:  
591 pushing the limits of fluorescence microscopy. *Nature Methods* **15**, 1090–1097.  
592 **Zuiderveld, K.** (1994). Contrast Limited Adaptive Histogram Equalization. In *Graphics*  
593 *Gems*, pp. 474–485. Elsevier.  
594  
595



## 596 **FIGURE LEGENDS**

### 597 **Figure 1: Pipeline overview for 3D image analysis of the whole ovary at larvae and** 598 **adult stages.**

599 (A) Fluorescent staining strategies for whole ovary imaging. Cytoplasmic  
600 autofluorescence from Histone H3 phosphorylation immunofluorescence (PH3) is used  
601 for larvae (left panel). Methyl-green (MG) nuclear staining delineating follicles contour is  
602 used for adult stage (right panel). Z-projection of raw data are shown (standard deviation  
603 method. Raw stacks sizes are indicated. (B) Image pre-processing steps used for  
604 reconstruction and enhancement, listed from top to bottom. (C) 3D segmentation step is  
605 performed with Cellpose algorithm. Adult images are subjected to several segmentations  
606 runs before and after image downscaling. (D) Image post-processing is performed for  
607 segmentation correction, label filtering and final quantitative analysis. Opensource tools  
608 are indicated in white boxes, deep-learning opensource tools in blue, commercially  
609 available software in red (AMIRA). Relative computation time for one sample is indicated  
610 (B-D). Voxel size is indicated in brackets (A-C). Scale bars 200  $\mu\text{m}$  (for larvae), 1000  $\mu\text{m}$   
611 (for adult), 100  $\mu\text{m}$  (for larvae inset), 500  $\mu\text{m}$  (for adult inset)

612

### 613 **Figure 2: 3D reconstruction of whole medaka ovaries.**

614 (A) Larvae ovary reconstruction with raw data. Total ovary size approach 1240  $\mu\text{m}$  in  
615 length (x), 630  $\mu\text{m}$  in width (y) and 515  $\mu\text{m}$  in height (z). XY plane at 188 $\mu\text{m}$  and XZ plane  
616 are shown with dotted lines. (B) XY plane showing PH3 staining and cytoplasmic  
617 background in oocytes at 188 $\mu\text{m}$  in depth, magnified in inset (D). (C) XZ orthoslice of  
618 larvae PH3 staining. A decrease in fluorescence intensity is observable near 400  $\mu\text{m}$  in  
619 depth. (E) Adult ovary reconstruction with raw data. Only back stack (dorsal face) is  
620 shown, with a size of 7645  $\mu\text{m}$  in length (x), 6033  $\mu\text{m}$  in width (y) and 2778  $\mu\text{m}$  in height

621 (z). XY and YZ virtual slices are shown with dotted lines. (F) XY plane at 1152 $\mu$ m depth  
622 shows MG staining resulting in delimited follicular contours, magnified in inset (H). (G)  
623 YZ orthoslice of dorsal face of adult ovary. Heterogeneity of MG staining is observable  
624 through depth. Scale bars 200 $\mu$ m (B, C), 50 $\mu$ m (D), 1000 $\mu$ m (F, G), 40 $\mu$ m (H).

625

626

627 **Figure 3: Image pre-processing for enhancement of features detection through**  
628 **larva ovary depth.**

629 (A) Representative 3D reconstruction of 20 dph (days post-hatching) larvae ovary before  
630 image processing. (B-E) Effect of successive image processing steps at 150  $\mu$ m depth and  
631 (B'-E') at 400  $\mu$ m depth assessed on XY cropped planes. A profile line intensity is used to  
632 assess fluorescence intensities nearby relevant objects to be segmented. Fluorescence  
633 intensity and signal to noise ratio are progressively enhanced. (F) 3D reconstruction of  
634 20 dph larvae after image pre-processing showing signal homogenization. Color gradient  
635 is representative of grey levels (1-255). Scale bar 100  $\mu$ m, Grid square size 50  $\mu$ m.

636

637 **Figure 4: Image pre-processing for enhancement of features detection through**  
638 **adult ovary depth.**

639 (A) Volume reconstruction of front and back adult z-stacks before image processing. (B-  
640 E) Effect of successive image processing steps at 780  $\mu$ m deep and (B'-E') at 2000  $\mu$ m deep  
641 assessed on XY cropped planes extracted on front stack. A profile line intensity is used to  
642 assess fluorescence intensities nearby relevant objects to be segmented. Fluorescence  
643 intensity loss in depth is greatly recovered and resolution of follicles contours is  
644 improved. (L) Final adult ovary reconstruction after 3D registration and image

645 enhancements. Color gradient representative of grey levels. Scale bar 300  $\mu\text{m}$ , Grid square  
646 size 500  $\mu\text{m}$ .

647

648

649 **Figure 5: Effect of image pre-processing on Cellpose 3D segmentation efficiency**

650 (A) XZ orthoslice of larvae ovary showing raw data and (C) image data after pre-  
651 processing, magnified on insets. (B) Cellpose segmentation output using raw data as input  
652 or (D) pre-processed image data. Results are shown after label erosion to correctly  
653 visualize labels individualization. Insets show more segmentation errors without image  
654 pre-processing, including unsegregated labels (arrows) or over-segmentation  
655 (arrowhead). (E) XY plane of adult ovary on raw data and (G) after image processing,  
656 magnified on insets. (F) Cellpose segmentation output for 30 pixel diameter using either  
657 raw data input or (H) pre-processed image. Segmentation results show high error number  
658 without image pre-processing, including many missing labels (arrowhead) especially in  
659 locations with heterogenous staining and high over-segmentation in medium and large  
660 size follicles. Scale bars: 200  $\mu\text{m}$  (A-D), 100  $\mu\text{m}$  (insets in A-D), 1000  $\mu\text{m}$  (E-H), 500  $\mu\text{m}$   
661 (insets in E-H).

662

663 **Figure 6: Post-processing corrections of segmented labels.**

664 (A, top) XY planes of 20 dph larvae ovary at  $\sim 330 \mu\text{m}$  depth showing pre-treated image  
665 data, Cellpose output, labels boundaries, eroded labels (subtracted boundaries) and final  
666 results after semi-automatic label filtration in AMIRA superimposed onto image data. (A,  
667 bottom) YZ planes for qualitative assessment of segmentation along Z-axis. Segmentation  
668 results after post-processing show good accuracy and shape fitting in XY or YZ planes with  
669 only few labels fusion for smallest oocytes (arrows) or missing label (arrowhead). (B, top)

670 XY planes of adult ovary at ~2500  $\mu\text{m}$  depth before and after Cellpose 30 segmentation.  
671 (B, bottom) YZ planes of adult ovary showing segmentation accuracy along Z axis. Largest  
672 follicles are over-segmented but other labels are correctly fitting follicles size. (C)  
673 Downscaled image data, Cellpose 30 segmentation results and post-processed images of  
674 adult data on XY plane (top) or YZ orthoslices (bottom). Large labels (stars) are combined  
675 to original scale segmentation result in (B) to replace segmentation errors of largest  
676 follicles. (D) Combined and filtered adult segmentation data superimposed onto image  
677 data. Labels show a good fit in size and shape of follicles at various sizes either on XY or  
678 YZ plane. Scale bars 100  $\mu\text{m}$  (larvae panels), 1000  $\mu\text{m}$  (adult panels).

679

680

681 **Figure 7: 3D Qualitative spatial visualization and quantitative analysis of ovarian**  
682 **content.**

683 (A) 3D ventral and dorsal reconstruction views of 20 dph larvae ovary, and (A') merged  
684 with segmented oocytes. Ovary size is approximately represented on bounding box  
685 measuring 1240  $\mu\text{m}$  in length (x, yellow), 630  $\mu\text{m}$  in width (y, green) and 515  $\mu\text{m}$  in height  
686 (z, red). (B) Oocytes spatial distribution visualized by diameter range from ventral and  
687 dorsal side of larvae ovary. Oocytes tend to localize dorsally through their growth. (C)  
688 Oocyte distribution in entire larvae ovaries (mean  $\pm$ SD, n=2) depending on their  
689 equivalent diameter. Diameter measure cut-off was applied at 25  $\mu\text{m}$ . Corresponding  
690 developmental stages of previtellogenesis are indicated: stage I, chromatin-nucleolar (25-  
691 60  $\mu\text{m}$ ) and stage II, perinucleolar (60-90  $\mu\text{m}$ ). (D) 3D ventral and dorsal views of entire  
692 adult ovary after registration and reconstruction, and (D') merged with 3D segmented  
693 follicles. Bounding box size approximates whole ovary size with an antero-posterior  
694 length of 7 mm (x, yellow), left to right width of 6 mm (y, green) and depth of 4,25 mm (z,

695 red). (E) Follicles spatial distribution within ovary based on their equivalent diameter  
696 range. Follicle size classes show respective localization of various developmental stages,  
697 namely previtellogenesis (50-150  $\mu\text{m}$ ), vitellogenesis (150-800  $\mu\text{m}$ ) and post-  
698 vitellogenesis (>800  $\mu\text{m}$ ). (F) Total quantification of adult ovarian content distributed by  
699 follicular diameter. Stages of development are listed, namely previtellogenesis (II-IV, 50-  
700 150  $\mu\text{m}$ ), early vitellogenesis (V-VI, 150-400  $\mu\text{m}$ ), late vitellogenesis (VII-VIII, 400-800  
701  $\mu\text{m}$ ) and post-vitellogenesis (IX, 800  $\mu\text{m}$  and over). Oocyte and follicular distribution are  
702 expressed as percentage of total objects counted within the ovaries.

703

704

705

706

707

708

709

710

711

712

713

714

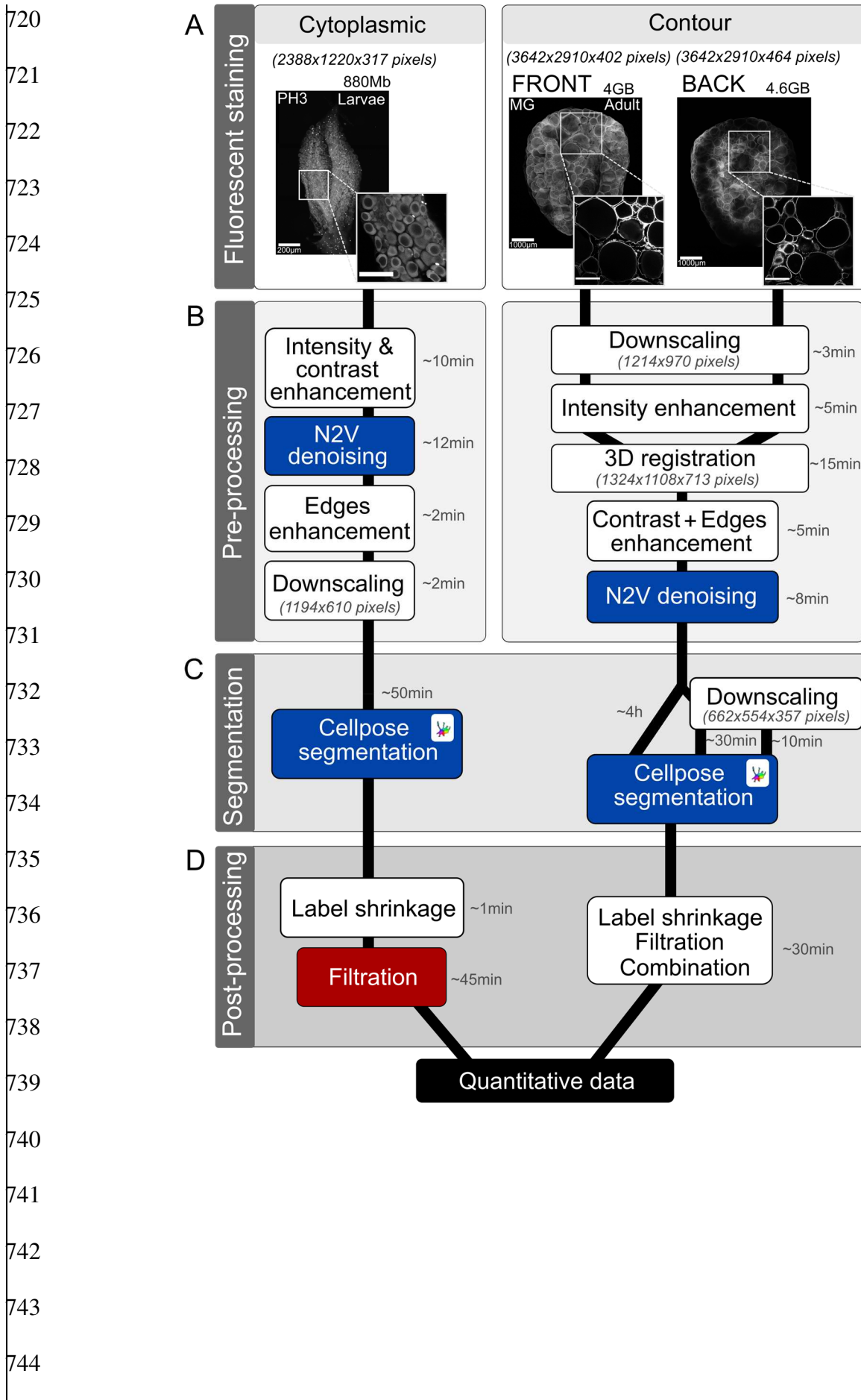
715

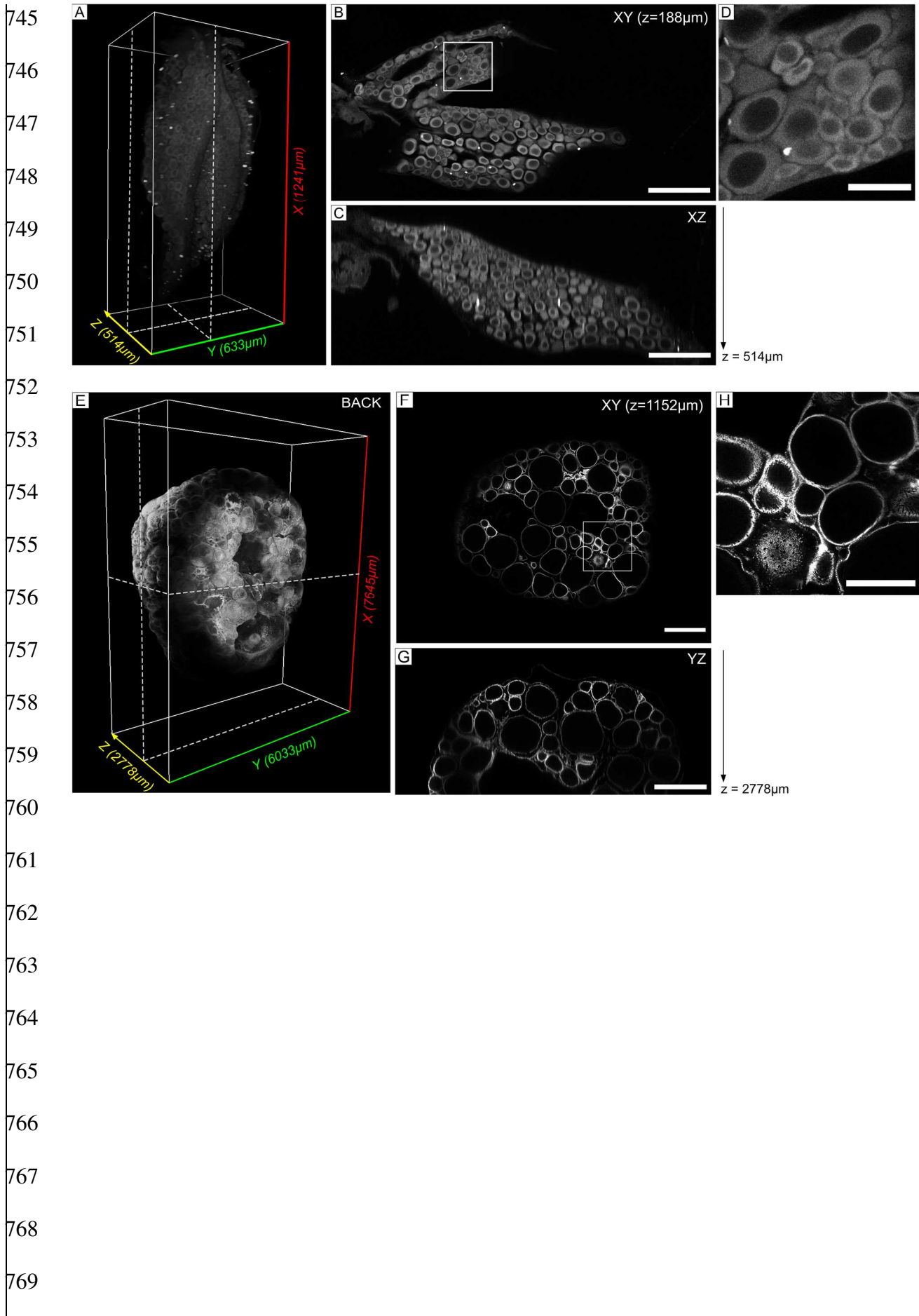
716

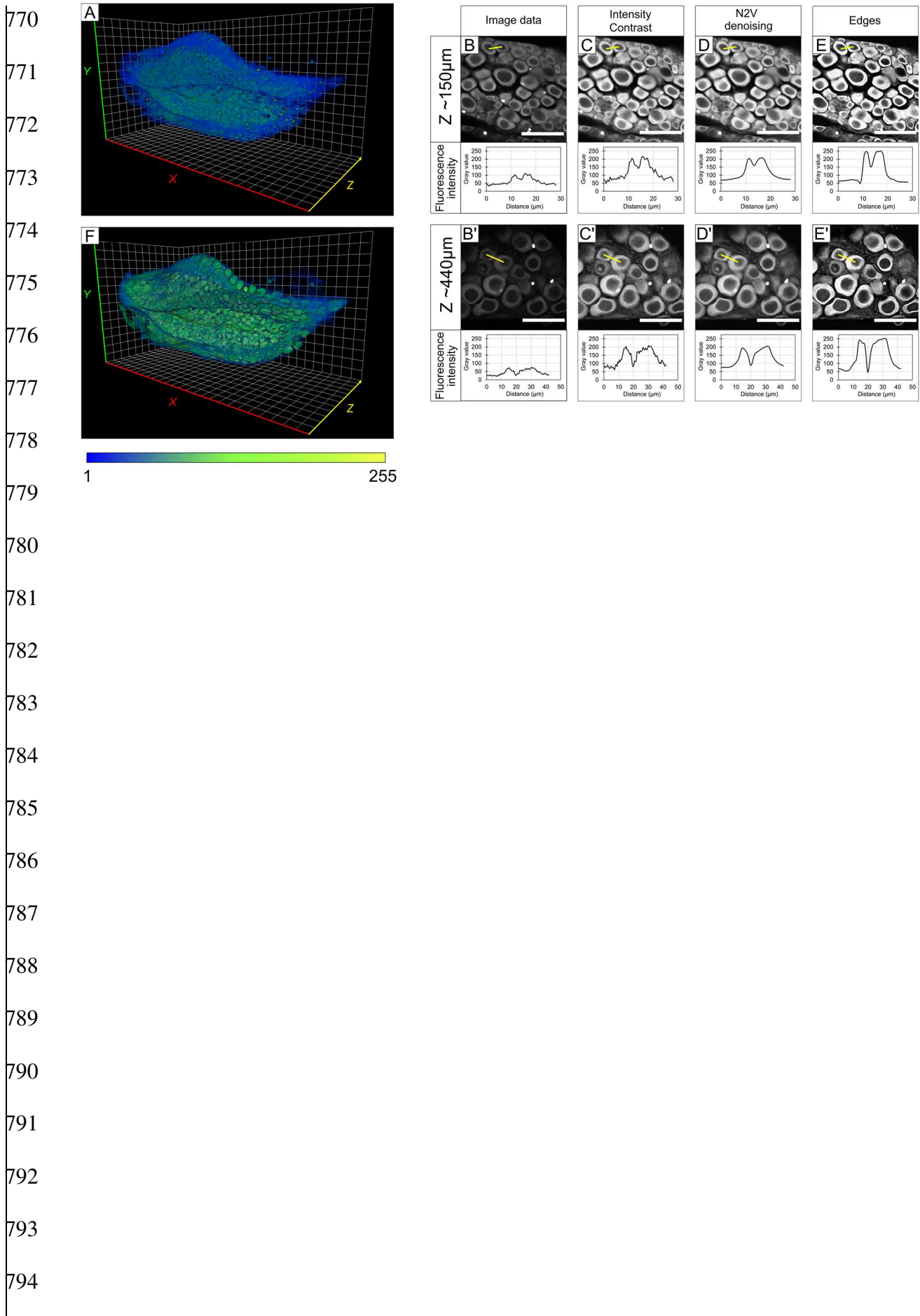
717

718

719









795  
796  
797  
798  
799  
800  
801  
802  
803  
804  
805  
806  
807  
808  
809  
810  
811  
812  
813  
814  
815  
816  
817  
818  
819

